ELSEVIER

Materials Science and Engineering A273–275 (1999) 40–57

MATERIALS SCIENCE & ENGINEERING A

www.elsevier.com/locate/msea

Martensite in steel: strength and structure

George Krauss *

Colorado School of Mines, Golden, CO 80401, USA

Abstract

This paper reviews the strengthening mechanisms associated with the various components of martensitic microstructures in steels and other ferrous alloys. The first section examines the experiments and strengthening theories associated with Fe–Ni and Fe–Ni–C alloys, in which the martensite, because of subzero M_s temperatures, can be evaluated with carbon atoms trapped in octahedral interstitial sites. The evaluation of strengthening in these alloys has been limited to interpreting yield strength of unaged, untempered martensite in terms of interstitial solid solution strengthening. The second section reviews strengthening of martensitic Fe–C alloys and low-alloy carbon steels with above-room-temperature M_s temperatures. In these alloys, it is impossible to prevent C diffusion during quenching, and strengthening of martensite becomes dependent on static and dynamic strain aging due to carbon atom interaction with dislocation substructure. In all alloys the dominant strengthening component of martensitic microstructures is the matrix of martensitic crystals, either in lath or plate morphology, but secondary effects due to other microstructural components such as carbides and retained austenite are also discussed.

Keywords: Martensite; Steels; Strengthening mechanisms

1. Introduction

Martensite in steels over the millennia has been used to do work, to do battle, and to support mechanical loads. Applications range from ancient elegantly crafted hand tools and swords [1,2] to current high-strength, high-fatigue resistant, high-wear resistant parts for machines, tools and dies, power transmission, gears and shafts, and demanding load-bearing structures such as aircraft landing gear. Hardened microstructures in steels require the generation of the parent phase austenite, the formation of martensite crystals by diffusionless, shear-type martensitic transformation, and adjustment of final strength and toughness by tempering. The essential atomic configurations do not change with time, but the combinations of phases, crystal morphologies, and crystal substructures in hardened steels are endless and the processing techniques to produce optimized microstructures continuously evolve, with surface hardening by induction, plasmas and lasers being the most recent innovations.

The purpose of this paper is to review the structural reasons for the high strength and hardness of martensite in ferrous alloys. Excellent state-of-the-art reviews regarding the origins of the strength of unaged or untempered martensite have been written by Cohen [3–5] and Owen [6], but because of the high mobility of carbon, the explanations developed have been based on experiments in iron–nickel–carbon alloys where carbon diffusion can be suppressed because of subzero Ms temperatures. Christian [7] has also reviewed the strength of martensite and effectively related it to the structural changes produced by the lattice and lattice-invariant deformations characterized by the crystallographic theory of martensitic transformation. In low-alloy steels and iron–carbon alloys, however, carbon diffusion cannot be suppressed, and to generate useable high-strength microstructures, is even promoted by low-temperature tempering. Thus the present review will take a broader view of the strength of martensitic microstructures, incorporating the many effects of carbon and as well as other phases and structures in hardened steels. Hardened microstructures in plain carbon and low alloy carbon steels are widely used, and scientific insights combined with experience gained in practical applications should help in defining the future performance limits of martensitic microstructures.

* Tel.: +1-303-6740670; fax: +1-303-6700797.
E-mail address: gkrauss@mines.edu (G. Krauss)

0921-5093/99/$ - see front matter
PII: S0921-5093(99)00288-9

This review will first describe the hardness and general carbon-dependent features of hardened microstructural systems in steels. Then the results of studies on Fe–Ni and Fe–Ni–C alloys will be reviewed. Finally, the properties and dynamics of deformation in hardened carbon steels will be discussed.

2. Hardness and microstructure of martensitic carbon steels

Fig. 1 shows hardness measured as a function of carbon content for a variety of carbon and low alloy steels by a number of investigators [8]. The references for the various investigations are given by their numbers in [8]. For a given carbon content, there is a wide range of hardness reported, typically on the order of 100 DPH units, for as-quenched steels. This scatter reflects differences in the multi-component systems which constitute the microstructures of hardened steels. Austenite grain size, which in turn affects the size of martensite crystals and the size of parallel arrays of martensite crystals, and thereby affects the strength of hardened microstructures, may vary. Varying amounts of retained austenite may also significantly affect hardness. The amount of retained austenite increases markedly with increasing carbon content, and may differ from one investigation to another. In fact some investigators have used cooling in liquid nitrogen to reduce the amount of retained austenite for the data plotted in Fig. 1, leading to the significant variations in hardness plotted for the high carbon steels.

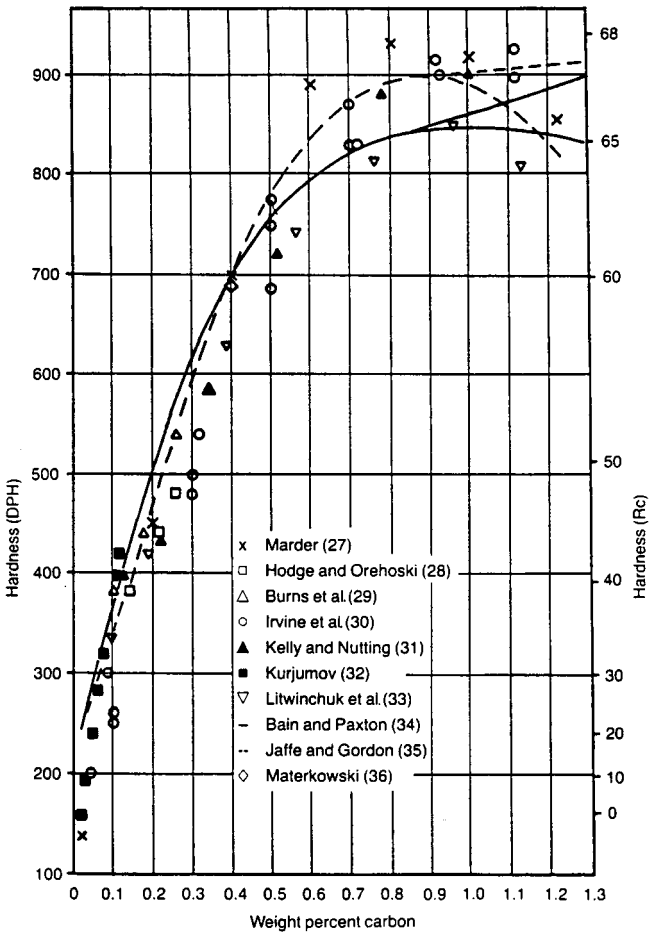

Fig. 1. Hardness of martensitic microstructures as a function of steel carbon content [8].

In addition to retained austenite, other phases which may be present in the microstructures of high-strength hardened steels may be fine carbides produced during quenching of low carbon steels with high Ms temperatures, i.e. carbides produced by autotempering, or transition carbides produced by low-temperature tempering [9]. On a somewhat larger size scale, spherical carbides undissolved during austenitizing prior to quenching, either because of insufficient time for the dissolution of carbides in the structures present prior to austenitizing [9–11], or by design in the intercritical austenitizing of hypereuctectoid steels, may also be a significant component of hardened microstructures. For example, in 52100 steel, a steel containing 1.00% C and typically austenitized in the two phase austenite–cementite field at 850°C, sufficient spherical carbides are retained to lower the carbon content of the austenite to 0.55% [12]. Thus, by virtue of the diffusionless martensitic transformation, the carbon content of the martensite in as-quenched 52100 steel is also 0.55%. Such variations in heat treatment practice make the direct relationship of hardness to the martensitic component of hardened microstructures of carbon steels difficult to interpret.

Coarse second-phase particles imbedded in martensitic matrices, either spheroidized carbides or inclusions, play a relatively small role in strengthening but play a major role in the fracture of hardened steels [9,11]. If the matrix martensite is capable of plastic flow and the second-phase particles are well dispersed, then the particles become the sites for microvoid formation and coalescence leading to ductile fracture. Other arrays of second-phase particles, such as carbides formed on austenite grain boundaries or between laths of martensite, may lead to brittle fracture and various types of embrittlement of hardened steels [10,13].

Despite the complexity of hardened microstructures, there is no question that the deformation response of the martensite crystals in as-quenched steels accounts primarily for the carbon-dependent hardness shown in Fig. 1. The complex interactions between the fine structure and the carbon atoms within martensite crystals under applied stress lead to the parabolic shape of the hardness versus carbon curve, and are the subject of many of the investigations described below. Based on recent nanohardness measurements on individual martensite crystals, the strengthening mechanisms which operate appear to extend to higher carbon levels

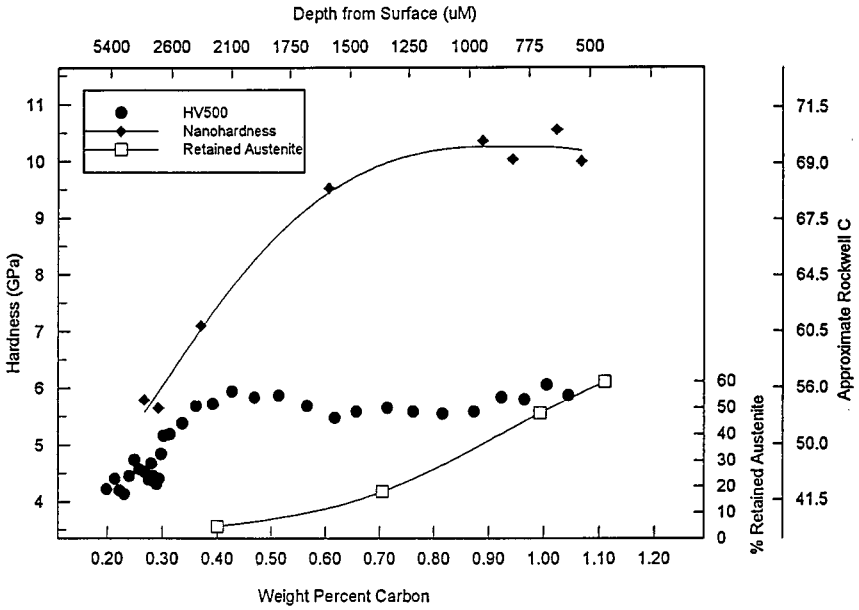

Fig. 2. Nanohardness, microhardness and retained austenite as a function of carbon content in a carburized and oil quenched 4320 steel [14].

than implied in Fig. 1 [14]. Fig. 2 compares the results of the nanohardness measurements to more macroscopic hardness measurements which integrate deformation response of larger volumes of the microstructure, including that of retained austenite as well as the martensite crystals [14]. The nanohardness measurements show that the hardness of individual plates of martensite attain and maintain very high values, close to HRC 70, at carbon contents of 0.80 wt.% C and above.

Although it is the deformation resistance of the carbon-containing substructure of martensitic crystals which accounts for the high hardness and strength of hardened steels, the shape and distribution of the crystals also contributes to the collective deformation behavior of hardened microstructural systems in carbon steels. Two major morphologies of martensitic crystals and microstructures, now termed lath and plate, form in steels [15–18]. Fig. 3 shows M_s as a function of carbon content and ranges of carbon content in which the lath and plate morphologies of martensite form [17,19,20]. Examples of light micrographs of lath and plate martensite are shown in Figs. 4 and 5 and discussed below.

Lath martensite forms in low- and medium-carbon steels and consists of parallel arrays or stacks of board- or lath-shaped crystals. In low-carbon alloys most of the crystals in a parallel group have the same crystal orientation and the parallel groups are referred to as blocks [21]. As carbon concentration increases, the parallel or almost parallel crystals in a group, termed packets, may have different orientations and variants of $\{557\}_A$ habit planes around a given $\{111\}_A$ plane [17,22–25]. The substructure of lath martensite produced by water or oil quenching consists of high densities of tangled dislocations, reflecting lattice invariant deformation and volume accommodation effects during athermal transformation from high temperatures. Recently, with the application of very high rates of cooling, at rates too high to permit dislocation motion, Schastlivtsev [20] has produced low-carbon martensite with twinned substructures. The high cooling rates depress the M_s temperatures, as shown in Fig. 3.

The parallel arrangement of crystals in lath martensite is apparent in Fig. 4, and the transmission electron microscope (TEM) is required to resolve all of the laths in a packet. Austenite is retained between the laths of martensite, as shown in Fig. 6, a dark-field TEM micrograph taken with a diffracted beam from the crystal structure of the austenite.

Plate martensite crystals form in non-parallel arrays and are characterized by irrational habit planes, including $\{3\ 10\ 15\}_A$, $\{225\}_A$ and $\{259\}_A$ [26]. The low M_s temperatures cause the plate martensite crystals to form at temperatures where the lattice invariant deformation is accomplished by twinning and limited dislocation motion. Often plate martensite crystals in high-carbon Fe–C alloys and steels may contain midribs, which appear as linear features in light micrographs, as shown in Fig. 5. In the TEM, the midribs have been shown to consist of closely spaced transformation twins. Outside of the central midrib area, the fine structure consists of dislocation arrays. Large amounts of retained austenite are typically present in plate martensite microstructures.

The morphology of martensitic microstructures affects deformation and strengthening in a number of ways. In lath martensites, the block and packet struc-

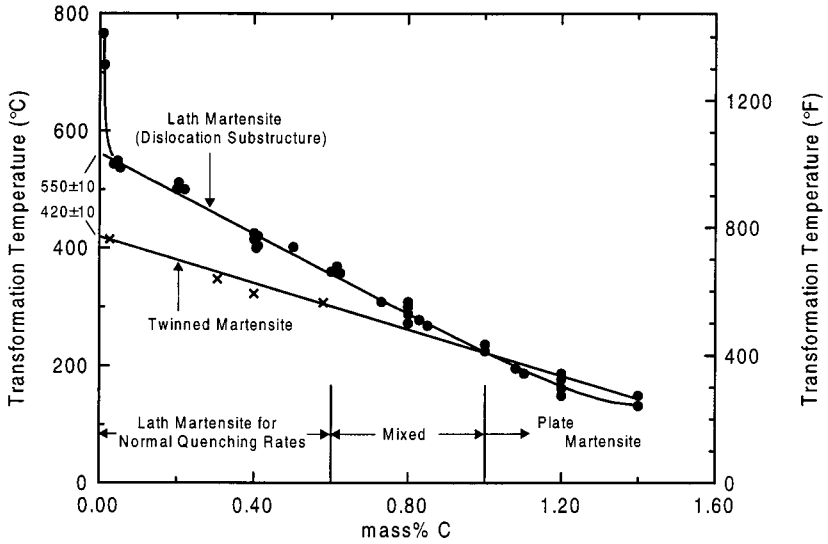

Fig. 3. Martensite start (M_s) temperatures and martensite morphology as a function of carbon content in Fe–C alloys [17,19,20].

tures, because of the largely common crystallographic orientation of the parallel component laths within the blocks and packets, become the effective grain structures which control deformation. Similarly, because of common $\{100\}_m$ cleavage planes in the parallel laths in blocks and packets, the size of cleavage facets under conditions which produce brittle transgranular fracture is directly related to packet size [27,28]. Also, the morphology of the retained austenite within lath and plate martensites determines if the austenite will mechanically transform by stress-induced or strain-induced mechanisms [29]. Also, the nonparallel formation of plate-shaped martensite crystals often results in intraplate microcracking due to the impingement of plates during quenching [30,31]. Examples of these microcracks are shown in a large martensite plate in Fig. 5. Some of these various effects of martensite morphology on deformation will be discussed in later sections of this review.

3. Strengthening mechanisms in Fe–Ni and Fe–Ni–C alloys

The strengthening mechanisms operating in as-quenched, unaged ferrous martensites have been thoroughly explored in Fe–Ni and Fe–Ni–C alloys by Winchell and Cohen [32,33] and Roberts and Owen [34–36] and summarized in the reviews referred to above [3–6]. Considerable effort was devoted to insuring that carbon atoms were indeed trapped in the set of octahedral sites of the martensite which derived directly from the octahedral sites which they occupied in the parent austenite. Any movement or segregation of carbon atoms to dislocations or interfaces or retained austenite or the rearrangement of carbon atoms into clusters or transition carbides was eliminated by selection of alloys with subzero M_s temperatures and mechanical testing at subzero temperatures. Fig. 7, from the work of Winchell, shows that maintaining temperatures below 60°C is necessary to prevent hardness changes caused by aging effects. Although at the time of Winchell experiments, the atomic-scale, carbon-dependent structural causes of the hardness changes were not known, there is now a considerable body of literature which documents a number of carbon atom rearrangements up to and through the transition carbide formation associated with low-temperature tempering [37–40].

In order to prevent carbon atom aging of as-quenched martensite, Winchell and Cohen evaluated Fe–Ni–C alloys with Ms temperatures around −35°C

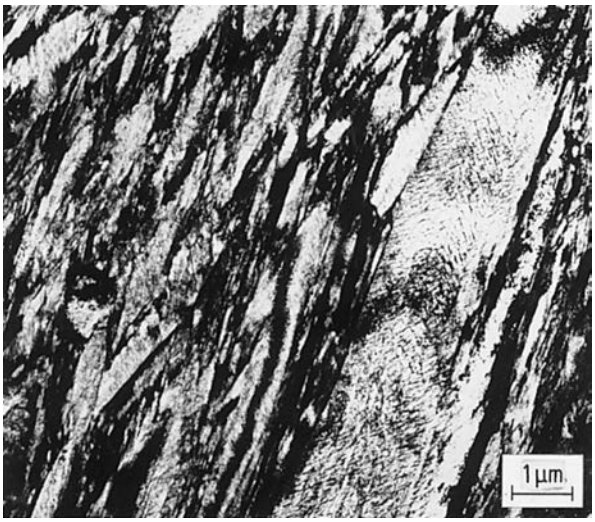

Fig. 4. Microstructure of lath martensite in 4140 steel tempered at 150°C. TEM bright field micrograph. Courtesy of J.M.B. Losz.

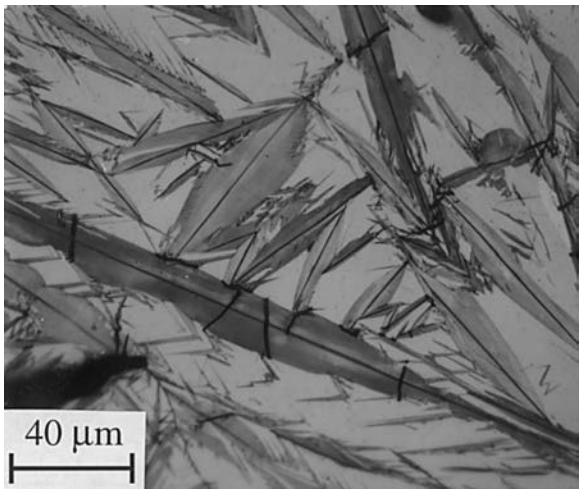

Fig. 5. Microstructure of plate martensite in an Fe–1.86 wt.% C alloy. Light micrograph. Courtesy of M.G. Mendiratta.

[32,33]. Since both C and Ni lower M_s temperatures, as carbon content was increased from 0.01 to 0.82 wt.%, Ni content was reduced from 30.5 to 16.7 wt.% in order to maintain constant subzero Ms temperatures for all of the alloys. The austenite of the Fe–Ni–C alloys, by virtue of their subzero transformation to martensite, transformed to plate martensite with largely twinned substructure and with large amounts of retained austenite, the amount of which depended on the quench temperature. Therefore, in order to obtain the flow strengths of fully martensitic microstructures, Winchell cooled each alloy to various temperatures, producing various amounts of retained austenite, and then after low temperature compression testing, extrapolated the flow stresses to 100% martensite, as shown in Fig. 8. Compression testing was necessary because the transformed alloys which contained more than 0.2 wt.% C failed by brittle fracture without appreciable plastic flow. As a result the Fe–Ni–C experiments do not provide mechanical properties, such as ultimate tensile strengths and ductilities, other than intercept flow stresses at low plastic strains.

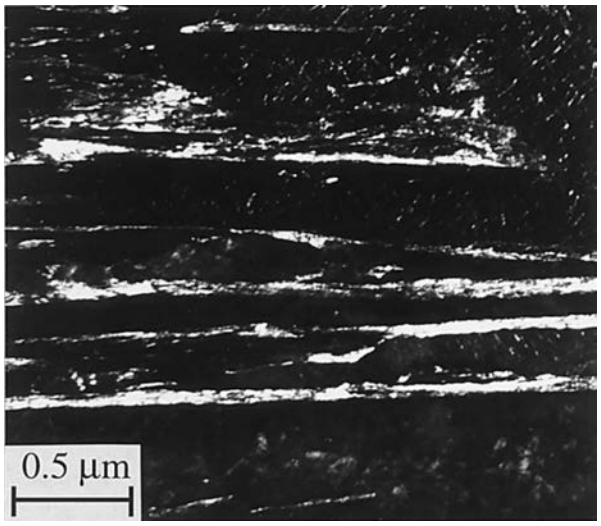

Fig. 6. Retained austenite (bright linear features) between laths of martensite crystals in a 4130 steel. Dark-field TEM micrograph. Courtesy of J.M.B. Losz.

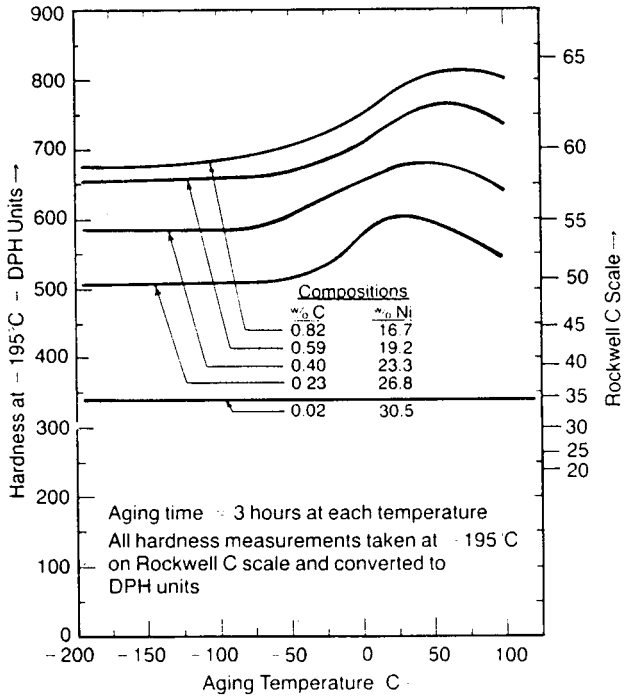

Fig. 7. Hardness of Fe–Ni–C martensitic microstructures at − 195°C after aging for 3 h at the temperatures shown [33].

Roberts and Owen broadened the matrix of Fe–Ni–C alloys to include a series with 21 wt.% Ni which transformed to lath martensite with a dislocation substructure [35]. Although the latter alloys transformed completely to martensite around 100°C, aging was suppressed by ice brine quenching and storing in liquid nitrogen prior to testing.

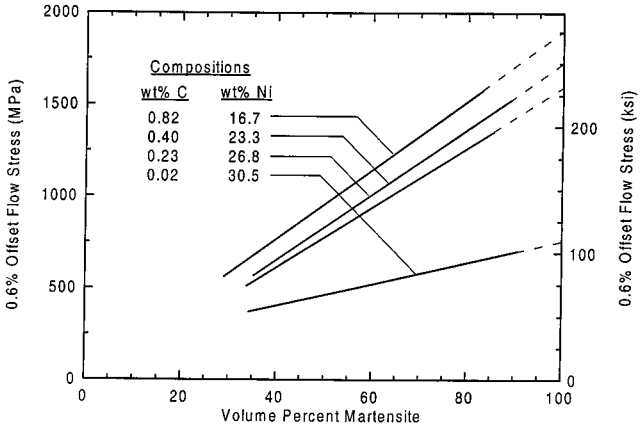

Fig. 8. Flow strength of martensite–austenite microstructures in various Fe–Ni–C alloys as a function of martensite content and extrapolation to 100% martensite [3,33]

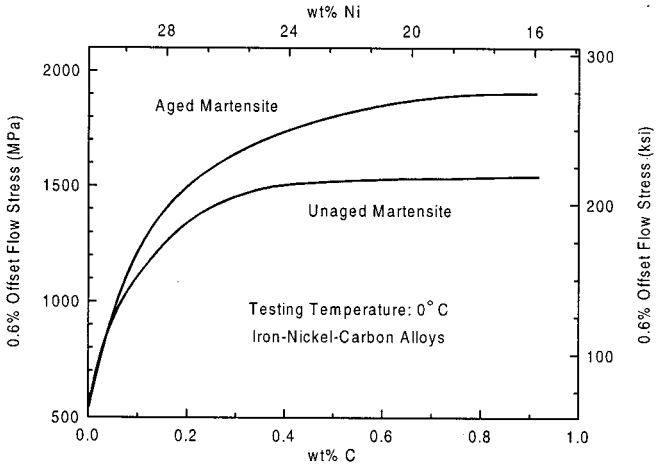

Fig. 9. Flow strength of martensite as a function of carbon content in Fe–Ni–C alloys [3,33].

Figs. 9 and 10 show results from the testing of the unaged martensitic microstructures in the Fe–Ni–C alloys. Fig. 9, after Winchell and Cohen [33], shows the parabolic dependency of the 0.6% offset flow stress on carbon content for both unaged and aged specimens. As the hardness data in Fig. 7 also shows, aging results in significant strengthening as carbon content increases. Based on arguments relating to the carbon atom distribution relative to the martensitic fine structure, Winchell and Cohen showed a cube root dependency of flow strength on carbon content. Later analysis showed a better fit of flow strength to the square root of carbon content, as shown in Fig. 10. Fig. 10 also shows the effect of strain hardening between 0.2 and 0.6% strain, indicating that strain hardening increases with increasing carbon content of the martensite.

Based on the 0.2% offset flow stress data of Fig. 10, the following equation was calculated for the carbon dependency of the strength of martensite [5]:

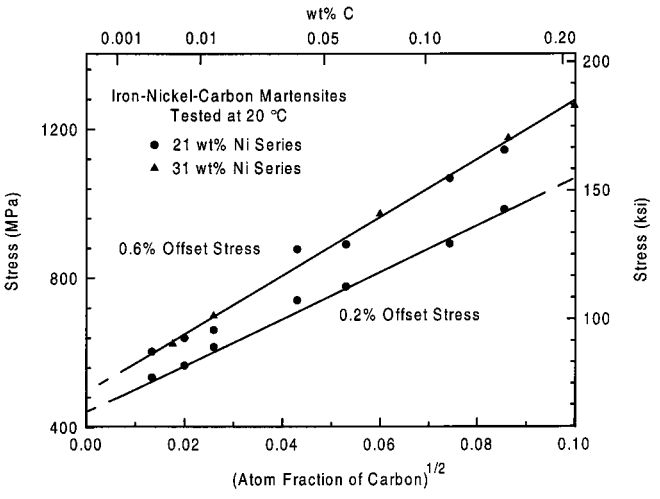

Fig. 10. Flow strength of martensite at 0.2 and 0.6% plastic strain as a function of the square root of carbon content [5].

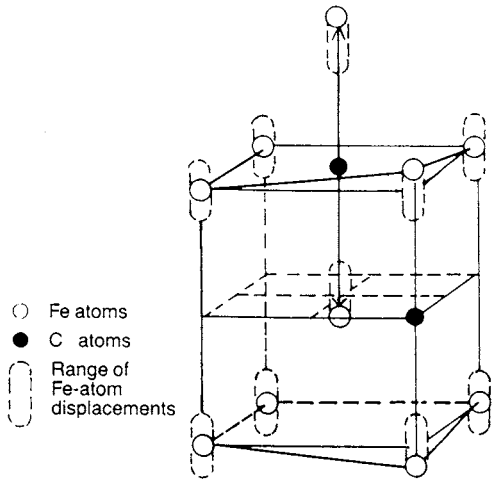

Fig. 11. Schematic representation of iron atom (open circles) displacements by carbon atoms (black circles) in tetragonal unit cell of martensite [3].

$$\sigma_{0.2}\ (\text{MPa}) = 461 + 1.31 \times 10^3\ (\text{wt.\% C})^{1/2} \quad (1)$$

The first term represents the flow stress of carbon-free martensite and includes contributions of Ni, estimated at 138 MPa for 20% Ni, the friction stress to move dislocations in pure bcc iron, estimated at 69 MPa, and the strengthening component of the substructure of martensite, estimated at 255 MPa. The latter terms are assumed constant as a function of carbon content, and therefore only substitutional strengthening by the carbon atoms in the interstitial octahedral sites accounts for the strong effect of carbon on the strength of martensite. The carbon atoms create substantial strains or displacements, termed dipole distortions [3], of the nearest neighbor iron atoms. Fig. 11 shows a schematic diagram of the iron atom displacements due to the carbon atoms. Thus if indeed carbon atom diffusion is suppressed by quenching and subzero storage and testing, the carbon atoms are trapped in the set of octahedral sites which produce the tetragonality of the martensitic crystal structure, and await the arrival of dislocations set in motion by the generation of critical resolved shear stresses during mechanical testing. The increasing interactions of the strain fields of moving dislocations with the increasing lattice strains due to the carbon atoms creates the strong dependency of the strength of unaged martensite on carbon.

In summary, the Fe–Ni–C experiments build a case for interstitial solid solution strengthening as the major strengthening mechanism for the increase in strength of unaged martensite with increasing carbon content. Owen discusses the various applicable theories of solid solution strengthening and concludes that dislocation pinning as a cause of the carbon strengthening is not a significant factor in unaged Fe–Ni–C martensites [6]. Similar to other body-centered cubic microstructures, for example polycrystalline ferrite in low-carbon steels,

unaged body-centered tetragonal martensites in Fe–Ni–C alloys [6] have a rapidly increasing thermal component of flow strength with decreasing temperature below room temperature. The thermal component of flow stress of Fe–Ni–C martensite, is independent of carbon content, and is attributed by Owen to a double kink mechanism of dislocation motion against the Peierls lattice stress. Other mechanisms of the strong temperature dependence of the flow stress of body-centered cubic structures include the thermally activated sessile–glissile transformation of screw dislocations which restricts the cross slip of screw dislocations and the associated dislocation multiplication required to sustain plastic deformation [41].

The data in Fig. 10 is based on microstructures with the two morphologies and substructures of martensite which form in ferrous alloys. There is little difference in the deformation behavior of the two types of martensite. Speich and Swann [42] specifically addressed the role that changing martensitic substructure plays in strengthening in a series of Fe–Ni alloys in which there is a transition in martensite morphology from lath to plate with increasing Ni content. Fig. 12 shows that there is a discontinuity in strength at around 4 wt.% Ni, but at higher Ni contents where the martensitic substructure undergoes a transition from a dislocation cell structure to a twinned structure there is no discontinuous change in yield strength. The discontinuity at low Ni contents is attributed to low hardenability which produces a non-martensitic substructure with random dislocations, and the balance of the strength increase is directly related to solid solution strengthening due to Ni atoms. Speich and Swann note that fine internal twinning in Fe–Ni plate martensites does not appear to be an important strengthening mechanism.

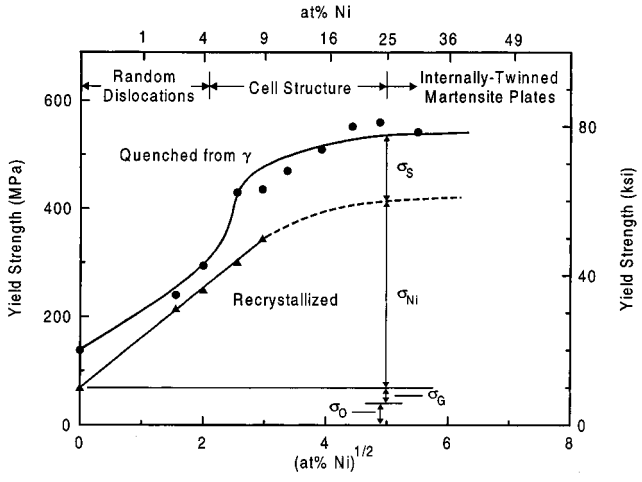

Fig. 12. Strength of martensitic microstructures as a function of Ni content in Fe–Ni alloys. The strength at low Ni contents is due to nonmartensitic microstructures [42].

In Fe–Ni–C alloys, similar to those studied by Winchell and Cohen, Richman has studied the plastic deformation modes in unaged plate martensites [43]. The unaged specimens were tested in compression at room temperature. Up to 0.05 wt.% C, deformation is entirely by wavy slip. With increasing carbon content, deformation twinning increases dramatically, until in martensites containing more than 0.4% C, deformation of the martensite crystals is entirely by mechanical twinning. A variety of twin orientations, including $\{112\}_m$, $\{013\}_m$ and $\{089\}_m$ was observed. The suppression of dislocation motion in the higher carbon Fe–N–C martensites may account for the brittleness noted above relative to the Winchell experiments, but the large amounts of retained austenite coexisting with plate martensites appear to insure at least some ductility even in high-carbon structures.

The results of the testing of the unaged martensitic microstructures in Fe–Ni and Fe–Ni–C alloys described above have used flow or yield stresses determined at plastic strains of 0.2 or 0.6% to establish strengthening behavior and the high strengths of carbon-containing martensites. Several investigations of unaged martensitic microstructures in the Ni-containing alloys, however, show that plastic deformation initiates at very low stresses in the microstrain regime. One explanation for this very low resistance to the initiation of plastic deformation is the fact that the substructure of the martensite crystals contains a very high dislocation density, and that therefore many dislocations will be available for slip at low stresses [44]. More detailed investigation has shown that the low-stress microplastic response at cryogenic temperatures is a result of the stress-induced transformation of retained austenite to martensite, and that the high flow stresses measured at plastic strains of 0.2% are a result of high rates of strain hardening due in part to the mechanical transformation of austenite in the microstrain region of deformation [45,46]. These experiments demonstrate that martensitic microstructures, even in the absence of aging and carbon diffusion, are indeed complex multiphase systems in which mechanical behavior depends not just on the martensitic phase.

4. Strengthening mechanisms in carbon and low-alloy steels

In carbon and low alloy steels with M_s temperatures well above room temperature the complete suppression of carbon diffusion during quenching is virtually impossible to attain. In the lowest carbon steels with high M_s temperatures, as shown in Fig. 2, carbon mobility is sufficient even to cause cementite precipitation in the martensite during quenching to room temperature, a process referred to as autotempering [47]. A more com-

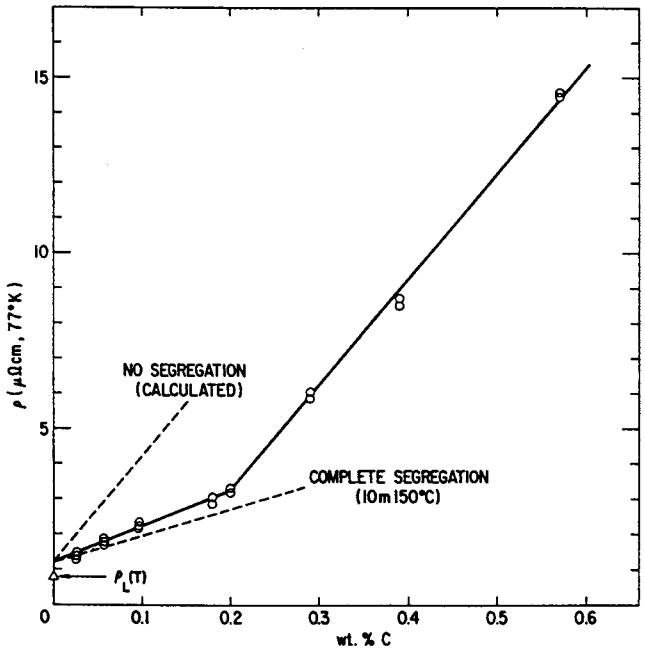

Fig. 13. Electrical resistivity of as-quenched Fe–C martensites as a function of carbon content showing effect of segregated carbon on the slope of the resistivity [48].

mon manifestation of carbon diffusion in martensite during quenching is segregation to dislocations and lath boundaries. Speich has presented indirect evidence for segregation in iron–carbon martensites based on the electrical resistivity measurements shown in Fig. 13 [48]. He reasoned that the lower slope of the resistivity curve for martensitic structures containing less than 0.2% C corresponded to complete segregation of the carbon to dislocations, leaving the ferrite free of the scattering centers due to C atoms trapped in octahedral interstitial sites. The higher slope of martensitic microstructures in steels containing more than 0.2% C was attributed to scattering by carbon atoms randomly distributed in the octahedral sites of the martensite. The measurement of increasing tetragonality of Fe–C martensite crystals with increasing carbon concentration by X-ray diffraction [49] certainly verifies that a significant fraction of carbon atoms are retained in octahedral sites in untempered higher carbon steels.

Direct evidence for carbon atom segregation to dislocations during quenching and room temperature aging of martensite has been obtained by Smith and his colleagues with field ion/atom-probe microscopy [50–52]. Fig. 14 shows the results of an Optical Position Sensitive Atom Probe (OPoSAP) analysis of carbon atom segregation around a dislocation line close to a screw orientation in lath martensite of an 0.18 wt.% C steel [52]. The carbon atom distribution appears to have three-fold symmetry, consistent with the carbon atom distribution about screw dislocations proposed by Cochardt et al. [53]. Smith et al confirm Speich's conclusion that almost 90% of the C atoms in a 0.18% C martensite are segregated to dislocations.

Several studies have been made of the carbon-dependence of the yield strengths of low-carbon martensites. Fig. 15 shows yield strength as a function of the square root of carbon content for martensitic specimens brine quenched and stored in liquid nitrogen before testing [54] The specimens were brine quenched and stored in liquid nitrogen before testing, but because of low hardenability even brine quenching was not sufficient to produce fully martensitic microstructures in the lowest carbon specimens. As a result there is a sharp drop in yield strength in steels with carbon contents below 0.013 wt.% C. Above 0.013 wt.% C, the yield strength increases directly with the square root of carbon content according to the following equation:

$$\sigma_{0.2}\ (\mathrm{MPa}) = 413 + 1.72 \times 10^3\ (\mathrm{wt.\%\ C})^{1/2} \quad (2)$$

The constant term on right side of the equation includes a factor for a constant substructure based on an average lath width of 0.25 μm, but Speich and Warlimont [54] conclude that theoretical treatment of the strengthening is difficult because of variations in substructure and the segregation of carbon to dislocations as a function of carbon content.

For even lower carbon steels, containing up to 0.058 wt.% C and Ni or Mn additions for hardenability, Norstrom has also found a square root dependency of as-quenched martensite yield strength on carbon content [55]. Fig. 16 compares his data to that of Speich and Warlimont. However, Nordstrom finds that dislocation density within the lath martensite increases with carbon content, similar to the findings of Kehoe and Kelly for Fe–C martensites [56], and that the dislocation density together with substitutional solid solution strengthening by Mn or Ni and packet size determine the yield strength rather than solid solution strengthening by carbon. The dislocation density measurements by Norstrom and Kehoe and Kelley are shown in Fig. 17, and the dependence of yield strength on packet size for various alloys are shown in Fig. 18. The low slope of the yield strength dependence on packet size for the alloys with the lowest carbon and highest Ni contents may be due to the known ability of Ni to promote cross slip of screw dislocations in bcc iron at low temperatures [57,58].

Norstrom developed an equation with the following terms for the yield strength of the low-carbon martensitic microstructures:

$$\sigma_y = \sigma_o + \sigma_1 + k_y D^{-1/2} + k_s d^{-1/2} + \alpha\ Gb\ [\rho_o + \mathrm{K}\ (\%\mathrm{C})]^{1/2} \quad (3)$$

where σ_o is the friction stress for pure iron, σ_1 is the solid solution strengthening from Mn and Ni, d is the lath width, D is the packet size, ρ_o is the dislocation density of martensitic pure iron, and the other terms

have their usual meaning. When experimental measurements for the various parameters and constants were used in equation [3], the calculated values of yield strength with carbon content agreed well with measured values.

Leslie and Sober [59] conducted an extensive study of carbon-dependent deformation behavior of martensitic microstructures in low-alloy carbon steels. The alloys included a series of steels based on AISI 4310, 4320, 4330 and 4340 grades, in which the content of Ni, Cr, and Mo were held constant at $\sim$1.8, 0.80, and 0.25 wt.%, respectively, and C was varied between 0.12 and 0.41 wt.%. The substitutional alloying elements provide good hardenability, the 4320 steel is an important commercial steel used for carburizing, and the 4330 and 4340 are widely used for high strength applications after quenching and low-temperature tempering. Leslie and Sober examined the tensile deformation behavior of untempered martensitic microstructures of the 43xx steels as a function of strain rate and testing at room temperature and below. Specimens were ice brine quenched from 900°C and immediately stored in liquid nitrogen until tested.

Fig. 19 shows, for the 4330 steel, an example of the data which Leslie and Sober obtained for the untempered martensitic microstructures [59]. Flow stresses at plastic strains of 0.2, 0.5, and 1.0% are shown, demonstrating significant strain hardening at all testing conditions. A significant thermal component of strengthening also develops with testing below room temperature. Evidence for dynamic strain ageing, i.e. carbon atom segregation to dislocations during testing, is shown by the negative strain rate sensitivity of the flow stress at room temperature. Leslie and Sober recognize that rearrangement of carbon atoms during quenching of the steels with M_s temperatures above room temperature results in a major structural component of untempered martensitic microstructures and, in the higher carbon steels, is the basis for a dominant strengthening contribution, much more so than solid solution strengthening by carbon atoms. As estimated by Leslie and Sober, Table 1 lists the contributions of the various strengthening components to the 0.2% yield strengths of the untempered martensitic 4310 and 4340 steels [41,59].

Dynamic strain aging, or the interaction of solute atoms with dislocations during plastic deformation, as detected by Leslie and Sober by negative strain rate sensitivity, has been the subject of systematic investigations in martensitic microstructures of Fe–Ni–C alloys by Roberts and Owen [60] and in a low carbon steel containing 0.14 wt.% C by Okamoto et al. [61,62]. In

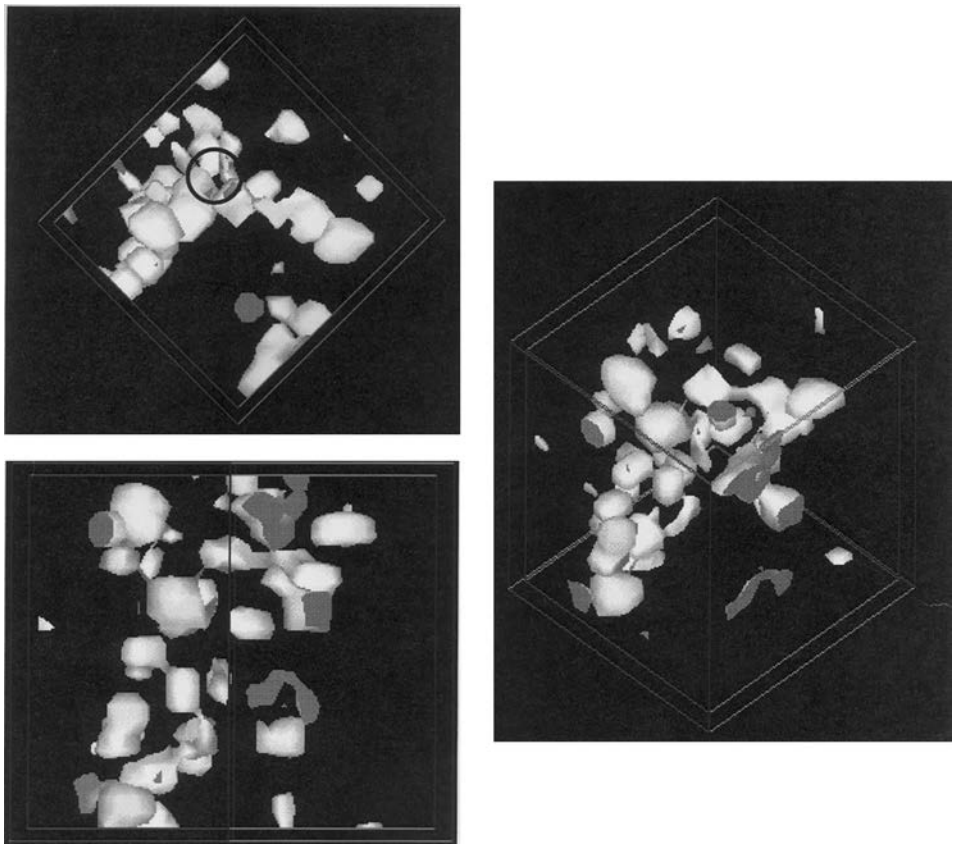

Fig. 14. Carbon atom distribution around dislocation in martensite of an Fe–0.18 wt.% C ally. Optical Position Sensitive Atom Probe analysis: various reconstructions from a region of analysis $10 \times 10 \times 4$ nm in size. Courtesy of J. Wilde and G.D.W. Smith.

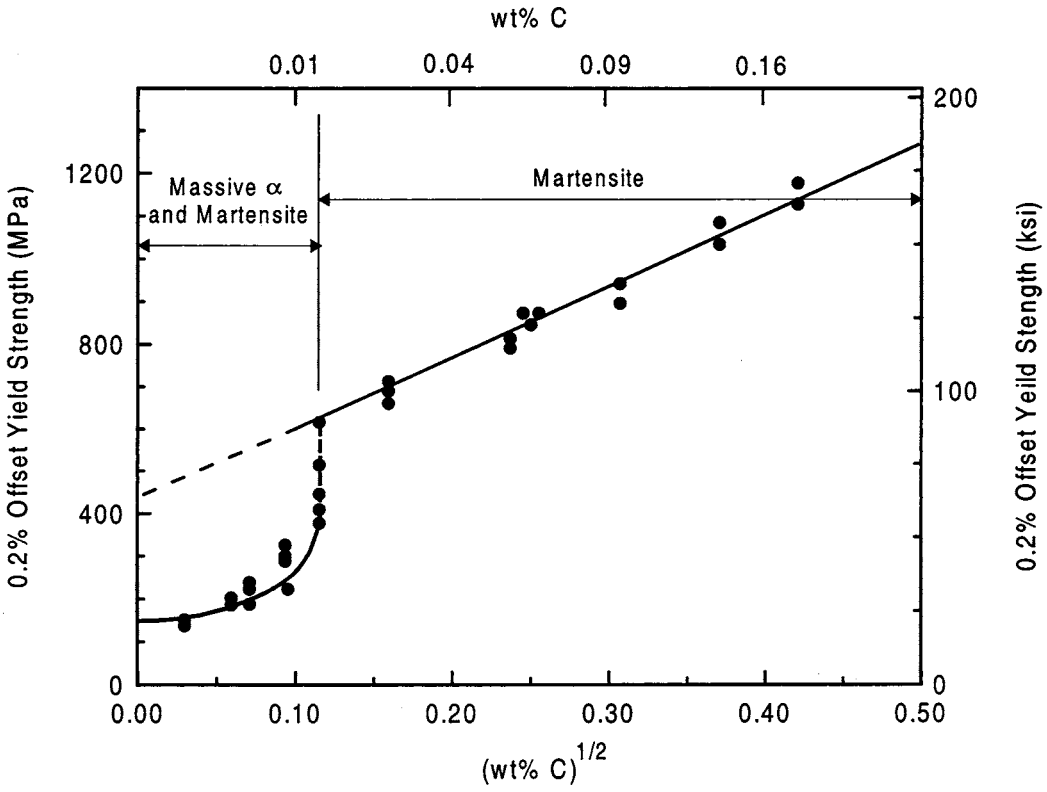

Fig. 15. Yield strength of martensitic microstructures as a function of carbon content in low carbon steels. The low strengths below 0.013% C are a result of low hardenability and nonmartensitic microstructures [54].

martensitic microstructures the dynamic strain aging manifests itself by serrated yielding, or sharp load drops in stress–strain curves. Such repeated discontinuous plastic flow is frequently referred to as the Portevin–Le Chatelier effect [63]. Fig. 20 shows an example of serrated plastic flow in the martensitic microstructure of the 0.14% C steel. Each drop in load was associated with a localized deformation band as shown in Fig. 21. The onset of serrated yielding is a function of strain rate and temperature of testing, and is characterized by activation energies of 77 and 81.1 kJ mol^{-1} in the 0.14% C steel [61,62] and Fe–Ni–C alloy [60] martensites, respectively, in good agreement with the activation energy for the diffusion of carbon in bcc iron [64].

Two explanations for the serrated yielding in carbon-containing martensites have been advanced. Roberts and Owen [60] propose that the discontinuous yield is caused by Cotrell atmosphere formation around dislocations and subsequent drag of the carbon atoms with moving dislocations to produce the stress drops. Okamoto et al [61,62] propose that the serrated yielding is caused by carbon atom segregation to screw dislocations, which when saturated with carbon atoms are unable to cross slip to generate the dislocations necessary to maintain continuous plastic deformation. The stress drops are caused by the generation of high densities of new dislocations at localized sites on the tensile specimens. In a constant strain rate test, the stress drop is explained [41,65] by the following equation

$$\dot{\varepsilon} = b\rho\bar{v} \tag{4}$$

where ε is the strain rate, b the Burgers vector, ρ the dislocation density, and $\bar{v}$ is the average dislocation velocity. With a discontinuous increase in dislocation

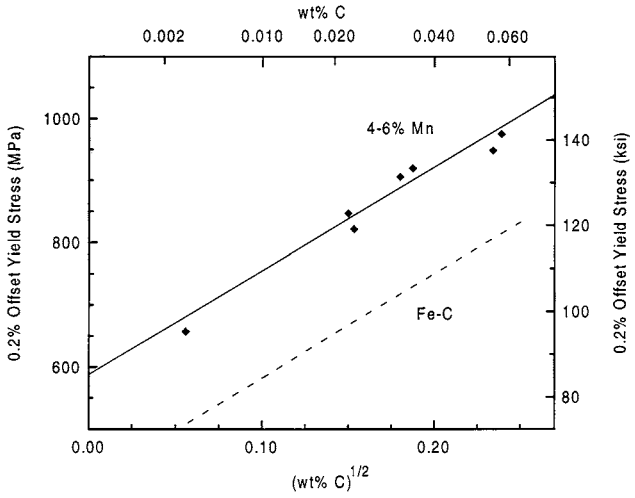

Fig. 16. Yield strength as a function of carbon content for Fe–Mn–C alloys [55]. Data for Fe–C alloys is from [54].

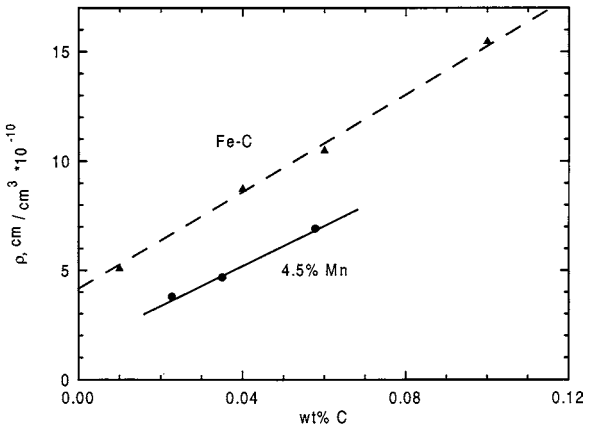

Fig. 17. Dislocation density in martensites of Fe–Mn–C alloys [55], and in Fe–C alloys [56].

density in a constant strain rate test, v, and therefore the stress to move dislocations, must drop.

The screw dislocation locking explanation of serrated yielding is based on the observation that only screw dislocations remain in specimens which have undergone the transition to serrated yielding. Fig. 22 shows residual screw dislocations in a specimen which developed serrated yielding after testing at 150°C at a strain rate of 8.3×10^{-4} s^{-1}. This dislocation substructure has replaced the high density of mixed edge and screw dislocations present in as-quenched lath martensite crystals in the 0.14% C steel. The transition in dislocation substructure implies that the quenched-in edge and mixed dislocations of the martensite provide the initial continuous plastic deformation as carbon segregates to screw dislocations. When the supply of mobile dislocations is exhausted, and only locked screw dislocations, unable to cross slip and generate new dislocations, remain, then discontinuous yielding occurs.

Many of the analyses of strengthening mechanisms in martensite discussed above have been based on a single

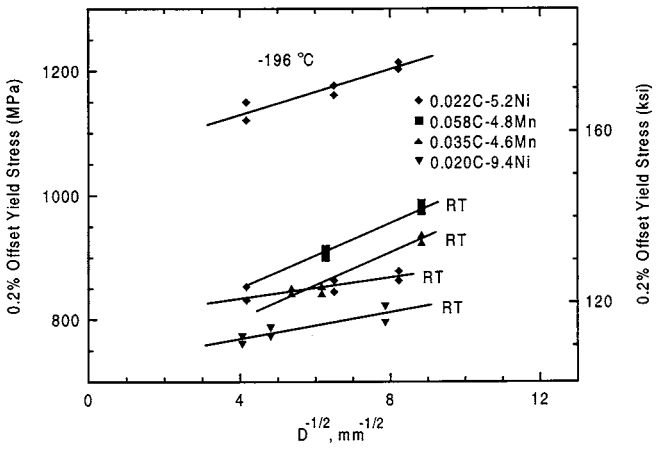

Fig. 18. Yield strength of Fe–Ni–C and Fe–Mn–C martensitic microstructures as a function of martensitic packet size (D) [56].

value of flow stress, often determined by compression testing. This approach has been necessary because of the susceptibility of high-strength martensitic microstructures to various types of embrittlement, and the fact that after a small amount of plastic deformation, stress-controlled fracture is initiated. However, the selection of and mechanical design with hardened steels requires microstructures not sensitive to embrittlement or an understanding of stress states and microstructural limitations which allow the use of fracture-sensitive steels for well defined applications. Thus an understanding of fracture mechanisms in hardened steel is equally as important as understanding the deformation mechanisms which define useable strength levels and which ultimately lead to fracture. A detailed review of the various mechanisms of embrittlement is outside of the scope of this paper, but a brief discussion of fracture is necessary to examine martensitic microstructures which have evolved to provide useful levels of high strength in carbon and low alloy steels.

Fig. 23 is a plot of fracture mechanisms of martensitic steels, under conditions of uniaxial or bending tensile stresses, as related to tempering temperature and steel carbon content [9]. The untempered microstructures discussed to this point are located in the area of Fig. 23 marked 'As-quenched Low Toughness Region'. Fig. 24 shows engineering stress–strain curves for untempered martensitic microstructures in 4330, 4340 and 4350 steels [66–68]. Only the 0.30 wt.% C steel shows ductile deformation behavior which leads to necking and eventual ductile fracture by microvoid formation and coalescence.

The stress–strain curve of the 4350 steel in Fig. 24 shows that it fractures with very little ductility and well short of necking instability. Examination [66–68] of the fracture surface of this specimen showed brittle intergranular fracture caused by phosphorus segregation and cementite formation on austenite grain boundaries prior to tempering [69]. This type of embrittlement dominates fracture of as-quenched and low-temperature tempered steels with greater than 0.5 wt.% C, as shown in Fig. 23. In order to differentiate this fracture from embrittlement mechanisms which develop on tempering, the intergranular fracture in as-quenched and low-temperature tempered martensites has been termed quench embrittlement [69].

The stress–strain curve of the as-quenched 4340 steel, Fig. 24, shows some plastic deformation, but also does not reach a maximum load which could be identified as an ultimate tensile strength. The fracture surface of this specimen consists of a mixture of cleavage facets and regions of microvoids. The deformation and fracture behavior of the as-quenched 4340 steel may be a result of dynamic strain aging similar to that discussed above for the 0.14 wt.% C martensite [61,62], with the higher carbon content of the 4340 martensite

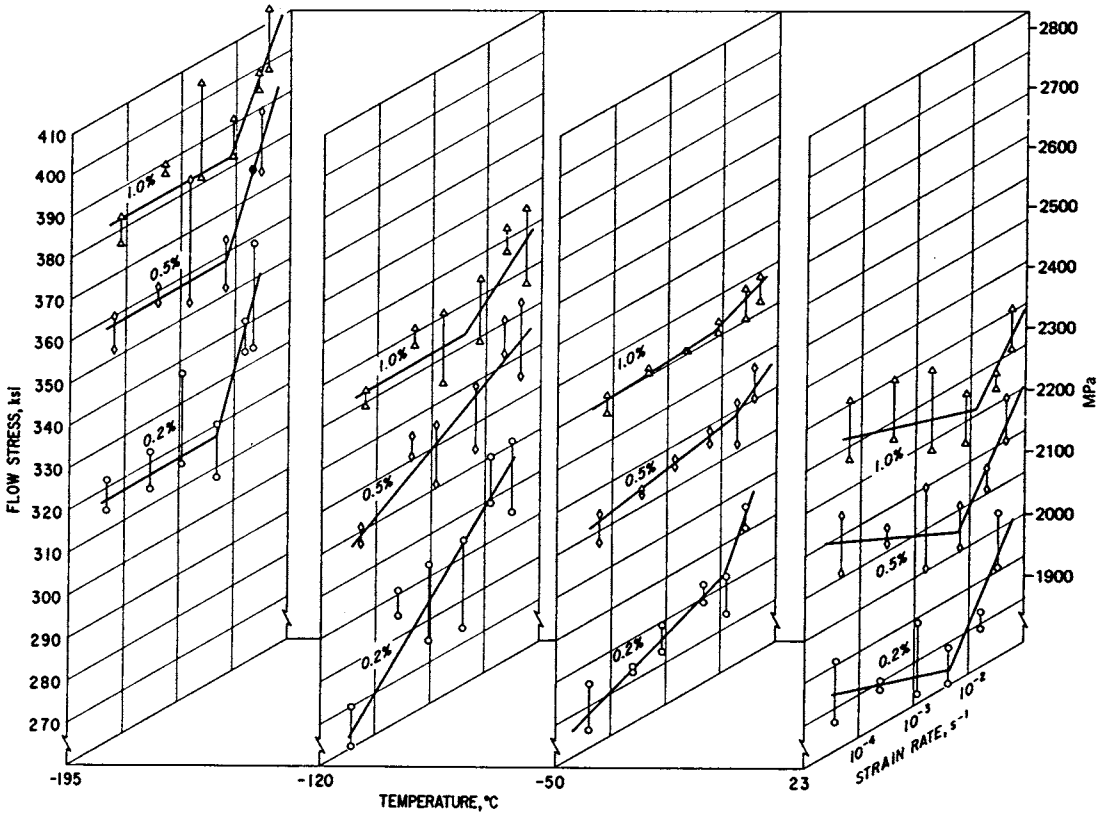

Fig. 19. Flow stress as a function of test temperature and strain rate for AISI 4330 quenched from 900°C [59].

driving critical levels of dynamic strain aging to room temperature [67,68].

In view of the inherent low toughness of as-quenched martensite in carbon steels, tempering, at least in higher-carbon medium–carbon steels, is necessary to exploit the high strength of martensitic microstructures. Industrially, to preserve as much of the strength of as-quenched martensite as possible, tempering is performed at low temperatures, between 150 and 200°C. Tempering at these temperatures for medium-carbon hardened steels containing up to 0.5 wt.% C results in ductile deformation and fracture behavior, as shown in Fig. 23. In steels containing more than 0.5 wt.% C, if quenched from temperatures in the single phase austenite field, the effects of quench embrittlement dominate even after low-temperature tempering and it is impossible to measure tensile properties [9].

Fig. 25 shows engineering stress strain curves for 41xx steels quenched to martensite and tempered at 150°C. All of the steels show ductile behavior: continuous, uniform plastic strain hardening, a maximum load which defines the ultimate tensile strength and the onset of necking instability, post uniform necking deformation, and ductile fracture by microvoid coalescence [9,11]. Figs. 26 and 27, show respectively, strength properties and ductility parameters taken from engineering stress–strain curves for martensitic specimens of 41xx and 43xx steels tempered at 150°C. The key to increasing strength of low-temperature tempered martensitic microstructures is the increased strain hardening with increasing carbon content. The higher strain hardening rates with increasing carbon content lead to higher uniform strains, as shown in Fig. 27, and defined by the following equation valid at maximum load in a tensile test.

$$\frac{d\sigma}{d\varepsilon} = \sigma \tag{5}$$

Table 1
Components of the strength of as-quenched martensite [41]

AISI 4310 (MPa)	Component	AISI 4340 (MPa)
620	Fine structure	620
205	Dynamic strengthening during the test	205
345	Work hardening	240
	Rearrangement of C atoms during quench	760
	Solid solution strengthening by C	415
1170	0.2% Offset yield strength	2240

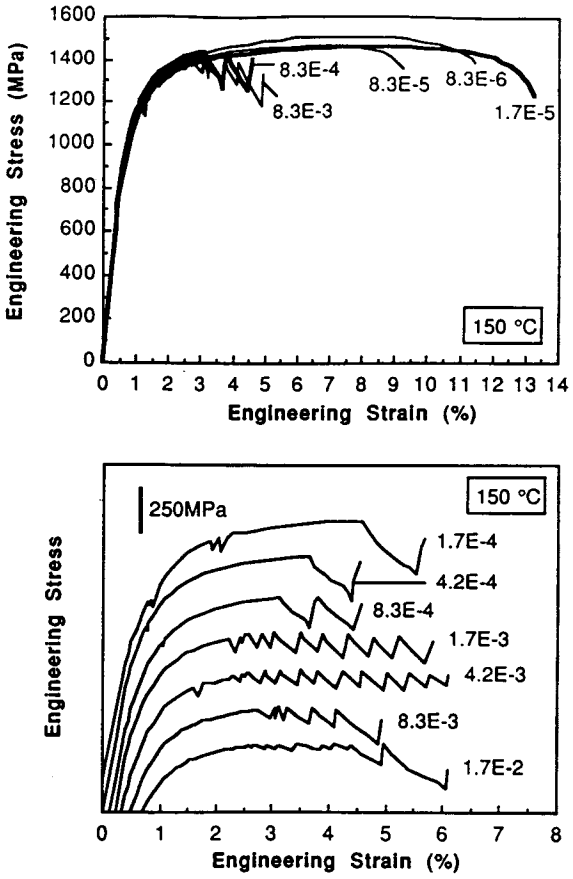

Fig. 20. Engineering stress–strain curves for as-quenched martensitic microstructures in 0.14 wt.% C steel tested at 150°C at various strain rates, top set of curves. Serrated yielding of 0.14 wt.% C martensite with stress axis displaced to show details of yielding, bottom set of curves [61].

where $d\sigma/d\varepsilon$ is the true strain hardening rate and σ is the true stress at necking [41]. Higher strain hardening rates as a function of strain, therefore, increase intersections with true stress–true strain curves to higher strains, increasing uniform strain or the onset of neck- ing instability [70,71]. The ductility parameters other than

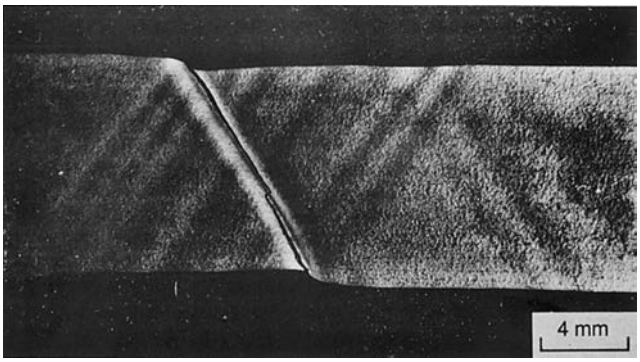

Fig. 21. Localized deformation bands in a sheet specimen of martensitic 0.14 wt.% C steel. Each band corresponds to a drop in load during serrated yielding [61]

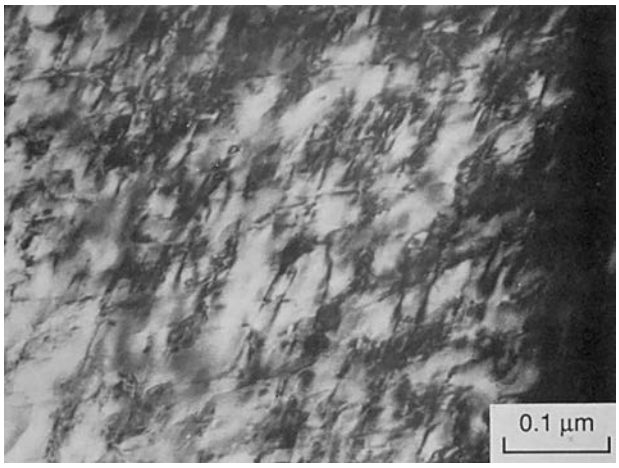

Fig. 22. Residual dislocation structure in a martensitic specimen of 0.14 wt.% C steel in which serrated yielding has developed during testing at 150°C [61].

uniform strain decrease with increasing carbon content because the high ultimate stresses of the high-carbon martensites are already close to the fracture stress. Therefore, little necking, which generates the post uniform strain, is required to generate ductile fracture stresses. The post uniform strain is also a major component of the total elongation and reduction of area.

Martensitic specimens tempered at temperatures between 150 and 200°C are solidly in the temperature range which produces the first stage of tempering. In this temperature range, fine transition carbides, on the order of 2–4 nm in size, precipitate within the martensite crystals [39,40]. As a result, many of the carbon atoms are tied up in carbide particles and are not available for dynamic strain aging. Also, the higher the carbon content of the martensite, the higher the density and the closer the spacing of the transition carbides and the transition carbide clusters [9,11,72]. Reduced lengths of carbon-free dislocation segments between the transition carbides would require higher stresses for plastic flow according to the work hardening theory of Kuhlmann–Wilsdorf [73,74]. That theory states that the flow stress, τ, at any given plastic strain is given by the equation:

$$\tau = \tau_o + \text{const } Gb/\bar{l} \quad (6)$$

where τ_o is the friction stress, $\bar{l}$ is the average momentary or active dislocation link length, and the other terms have their customary meaning. As flow stress increases, the average link length must continually decrease with increasing plastic strain to cause high rates of strain hardening. In tempered martensitic structures the dynamic interactions of dislocations with the transition carbides and the evolving dislocation substructure must generate finer and finer, l with increasing carbon content. The resulting dislocation substructure is very fine and its characterization requires further study. Also, the changing ratio of carbon atoms in solution, which may be

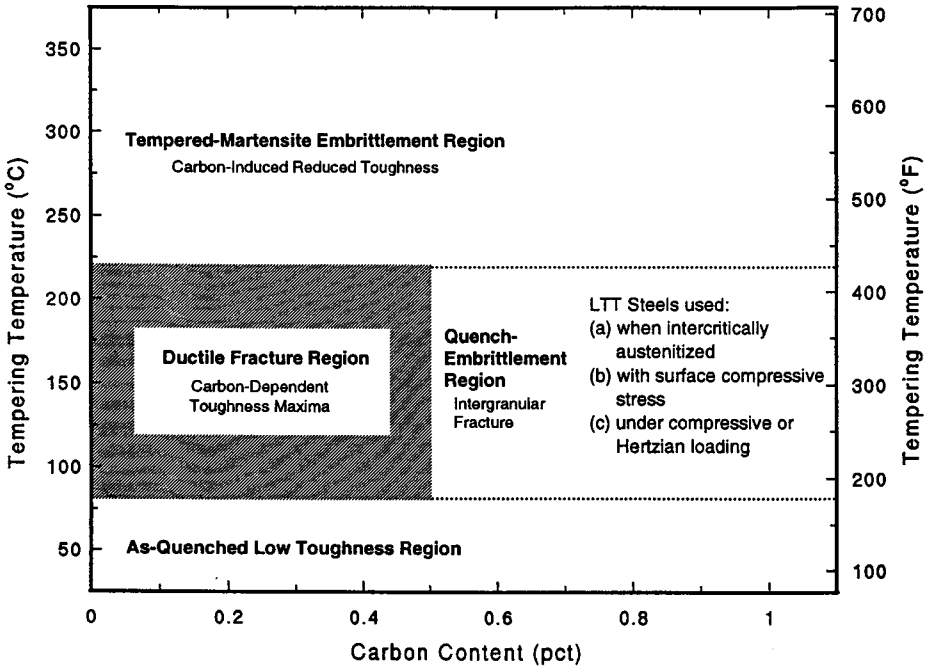

Fig. 23. Map of fracture mechanisms of martensitic microstructures as a function of tempering temperature and alloy carbon content [9].

available for dynamic strain aging, to those in transition carbide crystals, and changes in dislocation density due to recovery, as a function of changes in low-temperature tempering temperature and time are not well known. A recent study of the effects of changing tempering time and temperature during low temperature tempering shows that the deformation behavior of tempered 43xx martensites changes continuously with increased tempering in the first stage [66], an observation that indicates that the substructure must also be undergoing continuous change. Plastic flow of martensitic microstructures in FeNi alloys at strains in the microplastic range has been noted in the description of the Magee and Paxton and McEvily studies [44–46]. Similar microplastic flow at very low stresses has been noted in martensitic microstructures of Fe–C alloys and low-alloy carbon steels [72,75,76]. Figs. 28 and 29, from the work of Muir et al. show respectively, elastic limit, yield strength and ultimate tensile strength as a function of tempering temperature for specimens of a 0.41% C steel, and a summary of these properties as a function of hardness for 0.20. 0.41. and 0.82% C steels [75]. In the as-quenched and low-temperature tempered conditions, corresponding to the highest hardness values, the elastic limits are remarkably low. With increasing temperature, elastic limits increase to a maximum at a temperature close to the end of the first stage of tempering and the beginning of the second stage retained austenite transformation to ferrite and cementite. Muir et al. concluded that the low elastic limits of the as-quenched specimens were a result of internal stresses introduced by quenching to martensite [75].

Other work has also shown, in low-temperature tempered specimens of 4130, 4140 and 4150 steels, low elastic limits compared to yield and flow stresses determined at higher plastic strains. Fig. 30 shows elastic limits, in specimens tempered at 200°C, and flow stresses at various plastic strains in specimens tempered at 150°C, as a function of carbon content of the 41xx steels. The elastic limits decrease with increasing carbon content, opposite to the increase in flow stresses and ultimate tensile strength. The decreasing elastic limits correlate with increasing amounts of retained austenite with increasing carbon content [76]. Strain gage measurements of strain in the microplastic region show immediate strain hardening with the first measurable

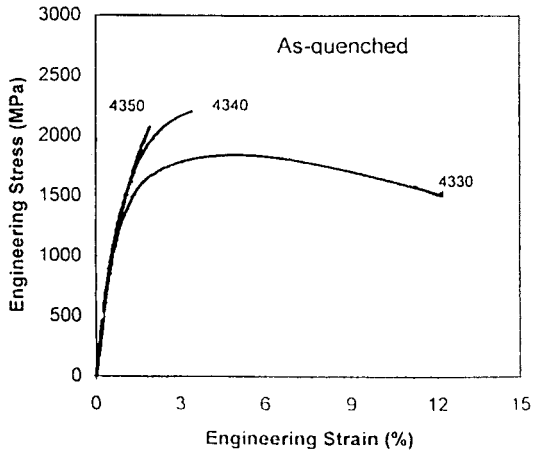

Fig. 24. Engineering stress–strain curves for untempered martensitic microstructures in 4330, 4340 and 4350 steels [66].

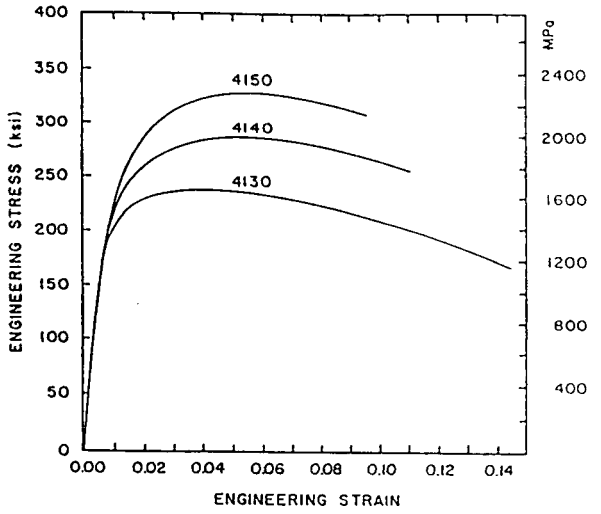

Fig. 25. Engineering stress–strain curves for 4130, 4140 and 4150 steel quenched to martensite and tempered at 150°C [11].

plastic strain, with the rate of strain hardening the highest in the 4150 specimens, Fig. 31. Retained austenite also decreased immediately [76], consistent with stress-induced transformation of austenite in lath martensite [29]. Thus plastic deformation begins at the lowest stress in the 4150 martensitic microstructure, but by virtue of the higher rates of strain hardening, the flow stresses at higher strains in the high-carbon 4350 steel are higher than those in the lower carbon microstructures. The higher rates of strain hardening persist as deformation shifts to the substructure of the tempered martensite crystals, leading to the highest ultimate tensile strengths in the 0.5% C steels as shown in Figs. 25 and 26.

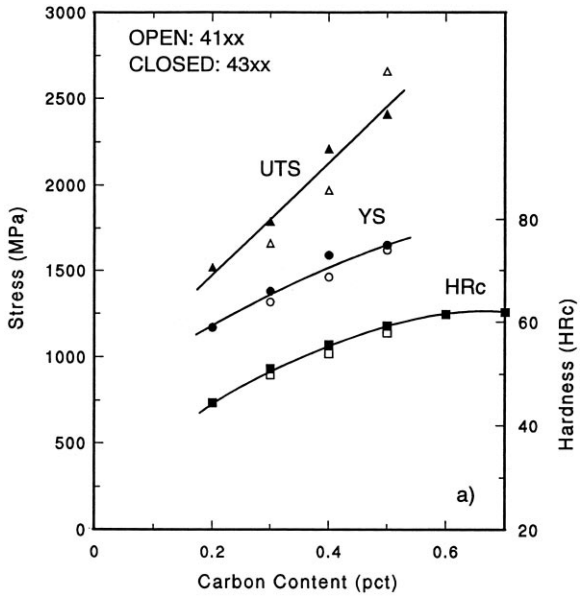

Fig. 26. Strength parameters of 41xx and 43xx steels, quenched to martensite and tempered at 150°C, as a function of carbon content [9].

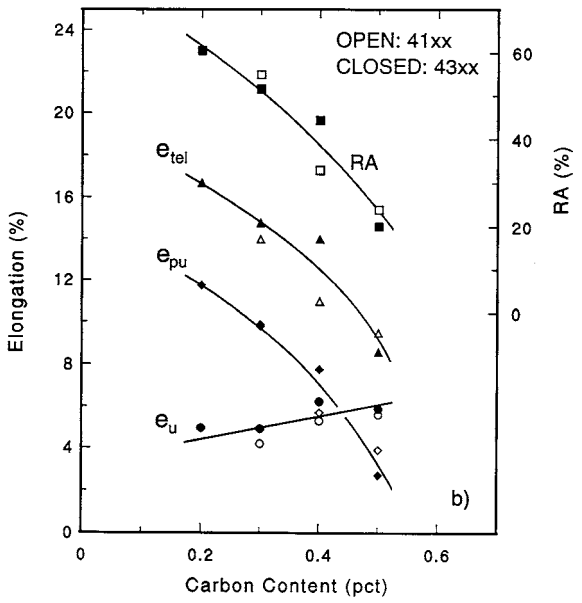

Fig. 27. Ductility parameters of 41xx and 43xx steels, quenched to martensite and tempered at 150°C, as a function of carbon content [9].

The discussion to this point has primarily considered the effect of the substructure of untempered and low-temperature tempered martensite crystals on strengthening. Austenite grain size also has an effect on the strength of martensitic microstructures, although it is superimposed on the substantial base deformation response of martensite crystals. Fig. 32 shows the dependence of the yield strength of several hardened low-alloy steels on austenite grain size. Although the austenite is mostly transformed to martensite, it influences deformation behavior because austenite grain size controls the size of martensite packets in medium-carbon steels which transform to lath martensite. The distribution of lath

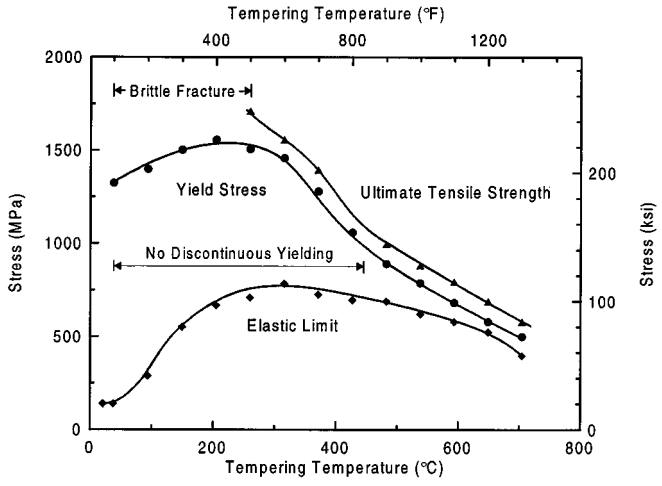

Fig. 28. Elastic limit, yield strength and ultimate tensile strength in an 0.41% C steel quenched to martensite and tempered at the temperatures shown [75].

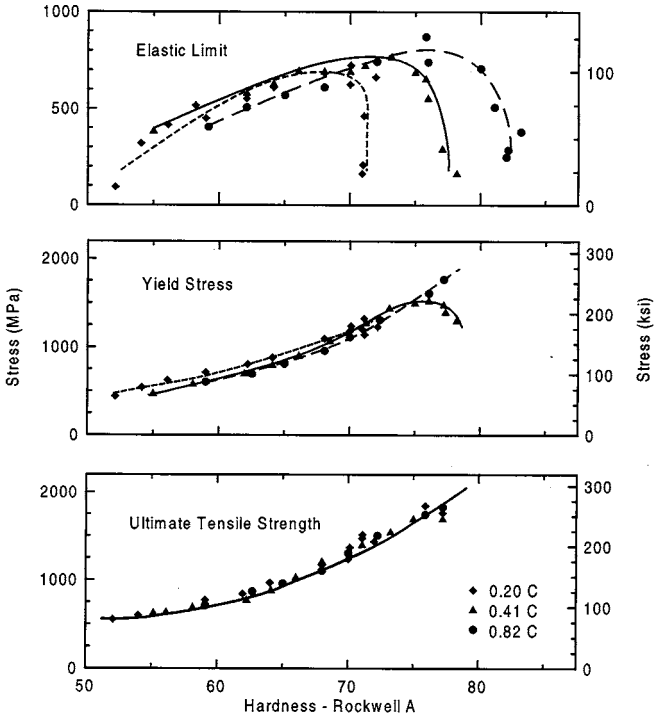

Fig. 29. Elastic limits, yield strength and ultimate tensile strength as a function of hardness for carbon steels containing various carbon contents and tempered at various temperatures [75].

sizes are generally the same within packets of the same size [16]. Fig. 33 shows, in a Hall-Petch type plot, the dependence of yield strength of martensite in an Fe–0.2 wt. C alloy on packet size. Also shown is the yield strength dependence of martensite on packet size in an Fe–Mn alloy [79]. The slope of the Fe–C martensite data is steeper than that of the Fe–Mn martensite, a

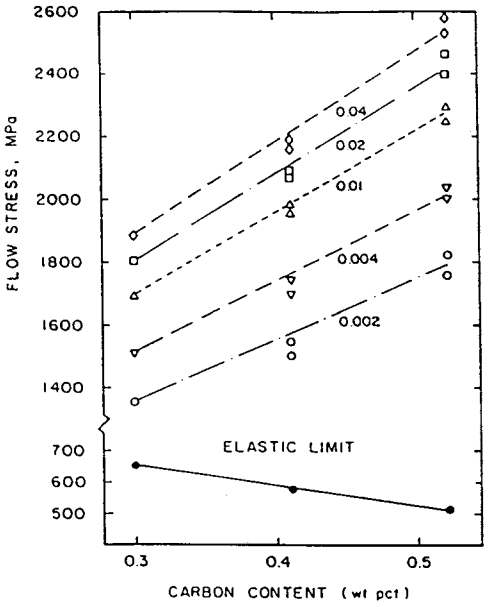

Fig. 30. Elastic limits and flow stresses at various plastic strains for quench and low-temperature tempered 41xx steels [72].

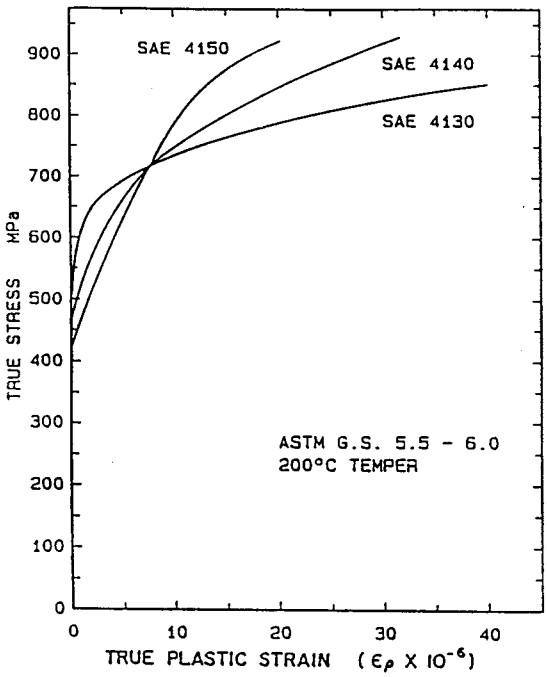

Fig. 31. Microplastic strain hardening of 4130, 4140 and 4150 martensitic microstructures tempered at 200°C. [76].

result attributed to C atom segregation to packet boundaries as well as to the dislocations and lath boundaries as discussed earlier.

5. Summary

The above review shows that many factors influence the strength of martensitic microstructures in steels and other ferrous alloys. While martensitic microstructures are complex, consisting of retained austenite and several possible levels of carbide distributions, in addition to martensite crystals of several morphologies, never-

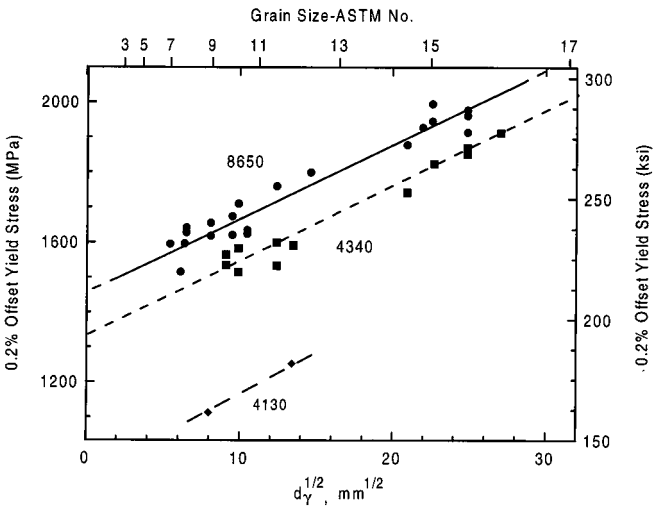

Fig. 32. Yield strength as a function of austenitic grain size of hardened low-alloy carbon steels [77].

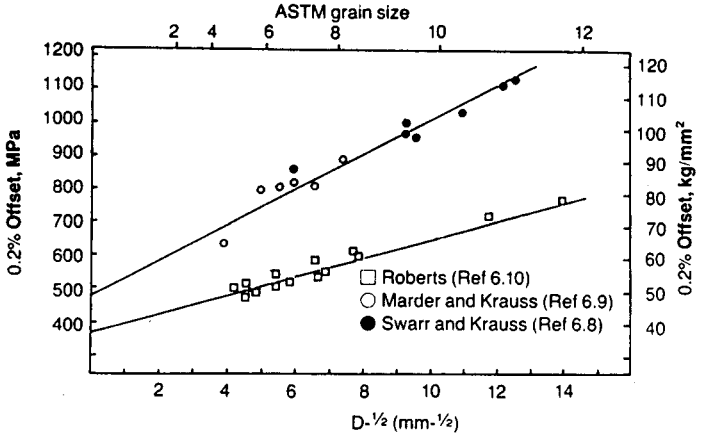

Fig. 33. Yield strength as a function of packet size, D, of lath martensite in an Fe–0.2 wt.% C Fe–C alloy and an Fe–Mn alloy [78]. References noted are given in [78].

theless it is the martensite which dominates performance. In the martensite crystals, the role that carbon atoms plays is varied, ranging from interstitial solid solution strengthening to segregation to dynamic strain aging, depending on whether or not carbon mobility can be suppressed during martensite formation and testing. The very high hardness of martensitic microstructures, and very high ultimate strengths if brittle fracture can be avoided, are very much a function of the dynamic interactions which lead to high rates of strain hardening during deformation. The atomic and substructural obstacles to dislocation motion in martensite are not fully characterized and require more research to provide deeper understanding of martensite deformation, mechanical properties, and fracture for future demanding structural applications.

Acknowledgements

The author is grateful to have been an observer and participant for almost 40 years in the search for understanding the structure and properties of martensite in steels. This review was written from that perspective and he acknowledges with respect the contributions of the many individuals cited and the contributions of his students and colleagues. Unfortunately, not all contributors to this search could be acknowledged, and other aspects of martensite remain to be discussed. The help of Kevin Smith and Bastiaan Cornelissen with the figures and Mimi Martin with the manuscript are acknowledged with thanks.

References

[1] R. Maddin, in: G.B. Olson, W.S. Owen (Eds.), Martensite, ASM International, Materials Park, OH, 1992, p. 11.
[2] L.S. Figiel, On Damascus Steel, Atlantis Arts Press, 1991.
[3] M. Cohen, Trans. AIME 224 (1962) 638.
[4] M. Cohen, J. Iron Steel Inst. 201 (1963) 833.
[5] M. Cohen, Trans. JIM, Supplement, 9 (1968) xxiii
[6] W.S. Owen, in: G.B. Olson, W.S. Owen (Eds.), Martensite, ASM International, Materials Park, OH, 1992, p. 277.
[7] J.W. Christian, in: A. Kelly, R.B. Nicholson (Eds.), Strengthening Methods in Crystals, Wiley, New York, 1971, p. 261.
[8] G. Krauss, in: D.V. Doane, J.S. Kirkaldy (Eds.), Hardenability Concepts with Applications to Steel, AIME, 1978, p. 229.
[9] G. Krauss, ISIJ Int. 35 (1995) 349.
[10] Z. Ebrahimi, G. Krauss, Acta Metall. 32 (1984) 1767.
[11] G. Krauss, Hart.-Tech. Mitt. 46 (1991) 7.
[12] J. Van, D Sanden, Pract. Metall. 7 (1980) 238.
[13] G. Krauss, C.J. McMahon, Jr., G.B. Olson, W.S. Owen (Eds.), Martensite, ASM International, Materials Park, OH, 1992, p. 295.
[14] J.D. Makinson, W.N. Weins, Y. Xu, R.J. DeAngelis, M.K. Ferber, L. Riester, R.V. Lawrence, in: K. Inoue, K. Mukherjee, K. Otsuka, H. Chen (Eds.), Displacive Phase Transformations and Their Application in Materials Engineering, TMS, Warrendale, PA, 1998, p. 391.
[15] P.M. Kelly, J. Nutting, J. Iron Steel Inst. 197 (1961) 199.
[16] G. Krauss, A.R. Marder, Metall. Trans. 2 (1971) 2343.
[17] A.R. Marder, G. Krauss, Trans. ASM 60 (1967) 651.
[18] A.R. Marder, G. Krauss, Trans. ASM 62 (1969) 957.
[19] E.A. Wilson, ISIJ Int. 34 (1994) 615.
[20] D.A. Mirzayev, V.M. Schastlivtsev, S. Ye Karzwnov, Fiz. Metal. Metalloved. 63 (4) (1987) 764.
[21] J.M. Marder, A.R. Marder, Trans. ASM 62 (1969) 1.
[22] T. Maki, K. Tsuzaki, I. Tamura, Trans. Iron Steel Inst. Jpn. 20 (1986) 207.
[23] B.P.J Sandvik, C.M. Wayman, Metall. Trans. A 14A (1983) 809.
[24] P.G. McDougall, C.M. Wayman, in: G.B. Olson, W.S. Owen (Eds.), Martensite, ASM International, Materials Park, OH, 1992, p. 59.
[25] P.M. Kelly, A. Jostsons, R.G. Blake, Acta Metall. Mater. 38 (1990) 1075.
[26] Z. Nishiyama, in: M.E. Fine, M. Meshii, C.M. Wayman (Eds.), Martensitic Transformation, Academic Press, New York, 1978.
[27] T. Inoue, S. Matsuda, Y. Okamura, K. Aoki, Trans. Jpn. Inst. Metals 11 (1970) 36.
[28] S. Matsuda, T. Inoue, H. Mimura, Y. Okamura, Trans. Iron Steel Inst. Jpn. 12 (1972) 325.
[29] G.B. Olson, in: G. Krauss (Ed.), Deformation, Processing, and Structure, ASM, Materials Park, OH, 1984, p. 391.
[30] A.R. Marder, A.O. Benscoter, Trans. ASM 61 (1968) 293.

[31] M.G. Mendiratta, J. Sasser, G. Krauss, Metall. Trans. 3 (1972) 351.
[32] P.G. Winchell, M. Cohen, in: G. Thomas, J. Washburn (Eds.), Electron Microscopy and the Strength of Metals, Interscience, 1963, p. 995.
[33] P.G. Winchell, M. Cohen, Trans. ASM, 55 (1962) 347.
[34] M.J. Roberts, W.S. Owen, Physical Properties of Martensite and Bainite, Iron and Steel Institute Special Report No. 93, 1965, p. 171.
[35] M.J. Roberts, W.S. Owen, J. Iron Steel Inst. 206 (1968) 375.
[36] M.J. Roberts, W.S. Owen, Trans. ASM 60 (1967) 687.
[37] M.K. Miller, P.A. Beaven, S.S. Brenner, G.D.W. Smith, Metall. Trans. A 14A (1983) 1021.
[38] S. Nagakura, Y. Hirotsu, M. Kusunoki, T. Suzuki, Y. Nakamura, Metall. Trans. A 14A (1983) 1025.
[39] G. Krauss, in: A.R. Marder, J.I. Goldstein (Eds.), Phase Transformations in Ferrous Alloys, TMS-AIME, Warrendale, PA, 1984, p. 101.
[40] G.R. Speich, K.A. Taylor, in: G.B. Olson, W.S. Owen (Eds.), Martensite, ASM International, Materials Park, OH, 1992, p. 243.
[41] W.C. Leslie, The Physical Metallurgy of Steels, McGraw-Hill, New York, 1981.
[42] G.R. Speich, P.R. Swann, J. Iron Steel Inst. 203 (1965) 480.
[43] R.H. Richman, Trans. TMS-AIME 227 (1963) 159.
[44] A.J. McEvily, R.C. Ku, T.L. Johnston, Trans. TMS-AIME 236 (1966) 108.
[45] C.L. Magee, H.W. Paxton, Trans. TMS-AIME 242 (1968) 1741.
[46] A.J. McEvily, R.C. Ku, T.L. Johnston, Trans TMS-AIME 239 (1967) 590.
[47] R.H. Aborn, Trans. ASM 48 (1950) 51.
[48] G.R. Speich, Trans TMS-AIME 245 (1969) 2553.
[49] C.S. Roberts, Trans. TMS-AIME 197 (1953) 203.
[50] M.K. Miller, P.A. Beaven, G.D.W. Smith, Metall. Trans. A 12A (1981) 1197.
[51] L. Chang, S.J. Barnard, G.D.W. Smith, in: G. Krauss, P.E. Repas (Eds.), Fundamentals of Aging and Tempering in Bainitic and Martensitic Steel Products, ISS-AIME, Warrendale, PA, 1992, p. 19.
[52] J. Wilde, M. Eng. Thesis, Department of Materials, Oxford University, 1996.
[53] A.W. Cochardt, G. Schoeck, H. Wiedersich, Acta Metall. 3 (1955) 433.
[54] G.R. Speich, H. Warlimont, J. Iron Steel Inst. 206 (1968) 385.
[55] L.-A Norstrom, Scand. J. Metall. 5 (1976) 159.
[56] M. Kehoe, P.M. Kelly, Scr. Metall. 4 (1970) 473.
[57] W. Jolley, Trans. TMS-AIME 242 (1968) 306.
[58] L.-A. Norstrom, O. Vingsbo, Metal Sci. 13 (1979) 677.
[59] W.C. Leslie, R.J. Sober, Trans. ASM 60 (1967) 459.
[60] M.J. Roberts, W.S. Owen, Metall. Trans. 1 (1970) 3203.
[61] S. Okamoto, D.K. Matlock, G. Krauss, Scr. Metall. Mater. 25 (1991) 39.
[62] S. Okamoto, D.K. Matlock, G. Krauss, in: C.M. Wayman, J. Perkins (Eds.), Proceedings of the International Conference on Martensitic Transformations, Monterey Institute of Advanced Studies, Carmel, CA, 1993, p. 451.
[63] A. Portevin, F. LeChatelier, Seanc. Acad. Sci. Paris 176 (1923) 507.
[64] A.S. Keh, T. Nakada, W.C. Leslie, Dislocation Dynamics, McGraw-Hill, New York, 1968, p. 381.
[65] G.T. Hahn, Acta Metall. 10 (1992) 133.
[66] M. Saeglitz, G. Krauss, Metall. Mater. Trans. A 28A (1997) 377.
[67] G. Krauss, in: K. Inoue, K. Mukherjee, K. Otsuka, H. Chen (Eds.), Displacive Phase Transformations and Their Applications in Materials Engineering, TMS, Warrendale, PA, 1998, p. 37.
[68] G. Krauss, Hart.-Tech. Mitt. 53 (1998) 147.
[69] R. S. Hyde, D.K. Matlock, G. Krauss, Proceedings of the 1998 Mechanical Working and Steel Processing Conference, ISS-AIME, Warrendale, PA, p. 921.
[70] D.K. Matlock, G. Krauss, F. Zia-Ebrahimi, in: G. Krauss (Ed.), Deformation, Processing and Structure, ASM, Materials Park, OH, 1984, p. 47.
[71] G. Krauss, D.K. Matlock, J. Phys. (France) IV 5 (1995) C8–51.
[72] Gu Baozhu, J.M.B. Losz, G. Krauss, Proceedings ICOMAT, The Japan Institute of Metals, 1986, p. 367.
[73] D. Kuhlmann-Wilsdorf, Metall. Trans. A 16A (1985) 2091.
[74] D. Kuhlmann-Wilsdorf, Mater. Sci. Eng. A113 (1989) 1.
[75] H. Muir, B.L. Averbach, M. Cohen, Trans. ASM 47 (1955) 380.
[76] M. Zaccone, G. Krauss, Metall. Trans. A 20A (1989) 188.
[77] R.A. Grange, Trans. ASM 59 (1966) 26.
[78] T.E. Swarr, G. Krauss, Metall. Trans. A 7A (1976) 41.
[79] M.J. Roberts, Metall. Trans. 1 (1970) 3287.